

# Electrochemical impedance spectroscopic characterization of the oxide film formed over low modulus Ti–35.5Nb–7.3Zr–5.7Ta alloy in phosphate buffer saline at various potentials

Shaily M. Bhola · Rahul Bhola · Brajendra Mishra · David L. Olson

Received: 5 April 2010/Accepted: 11 June 2010/Published online: 23 June 2010  
© Springer Science+Business Media, LLC 2010

**Abstract** Electrochemical impedance spectroscopic characterization of the low modulus Ti–35.5Nb–7.3Zr–5.7Ta alloy has been performed in phosphate buffer saline solution at 37 °C. Measurements were performed at various immersion intervals up to 720 h at OCP and also at various anodic potentials up to 2 V. The alloy exhibits a two time constant impedance response at the OCP and a one-time constant response at anodic potentials in the passive region. The thickness of the oxide film formed has been evaluated and the electrochemical interpretation of the results has been reported. Cyclic potentiodynamic profile of the alloy displays valve metal characteristics and the presence of a wide passive region that extends up to the maximum potential value of 2 V studied.

## Introduction

Titanium alloys are the most preferred choice for use as biomaterials because of their well acknowledged superior properties over other materials. Of late, there has been concern with the use of  $\alpha + \beta$  Ti–6Al–4V, the most widely used biomaterial due to reasons known [1–7]. New titanium alloy compositions specifically tailored for biomedical applications have been developed, amongst which the minimum elastic modulus has been achieved by the  $\beta$  Ti–Nb–Zr–Ta (TNZT) system [8–12]. Moreover, the TNZT alloys offer an opportunity of minimizing adverse tissue reaction through the restricted use of biocompatible Nb, Zr, and Ta [13, 14].

Recently, studies have been carried out on the influence of potential on the electrochemical behavior of Ti–29Nb–13Ta–4.6Zr alloys in Hanks solution [10, 15]. The aim of this investigation is to study the electrochemical response of Ti–35.5Nb–7.3Zr–5.7Ta alloy in phosphate buffer saline solution at the steady state and various anodic potentials and to hence elucidate the changes in oxide morphology of the passive film under these conditions from EIS circuit modeling.

## Experimental

Titanium alloy Ti–35.5Nb–7.3Zr–5.7Ta (TNZT) (composition in wt%: 0.05% C, 0.05% Fe, 0.015% H, 0.02% N, 0.15% O, 35.5% Nb, 5.7% Ta, 7.3% Zr, and 51.21% Ti) was used for the present electrochemical investigation in phosphate buffer saline (PBS) solution (0.137 M sodium chloride, 0.0027 M potassium chloride, and 0.01 M phosphate buffer) at 37 °C.

A three-electrode cell assembly consisting of TNZT alloy as the working electrode, platinum wire as the counter electrode and a saturated calomel electrode as the reference electrode was used for the electrochemical measurements. The DC electrochemical measurements were conducted using a PAR Potentiostat 273A and for the AC measurements, a PAR 1255 FRA was used in addition to the potentiostat. The open circuit potential (OCP) values of the alloy were monitored with time from immersion up to 720 h. Cyclic polarization measurements were performed at 168 h of immersion by polarizing the alloy specimen from –250 mV versus the OCP up to a vertex potential of 2 V versus the reference electrode, after which the scan was reversed and the final potential was the same as initial potential. The scan rate of 1 mV/s was used for

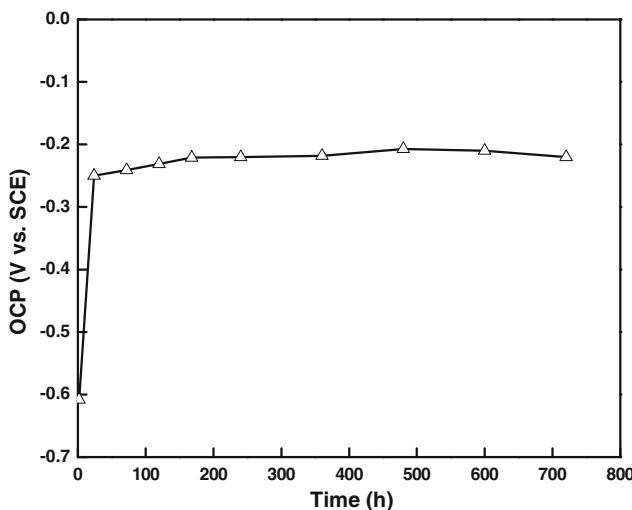
S. M. Bhola (✉) · R. Bhola · B. Mishra · D. L. Olson  
Department of Metallurgical and Materials Engineering,  
Colorado School of Mines, Golden, CO 80401, USA  
e-mail: sbhola@mines.edu

the polarization sweep. Electrochemical impedance spectroscopy (EIS) measurements were performed at the OCP for various intervals up to 720 h. At the end of 720 h, the impedance measurements were performed at various anodic potentials up to 2 V. The frequency sweep was applied from  $10^5$  to  $10^{-2}$  Hz with the AC amplitude of 10 mV.

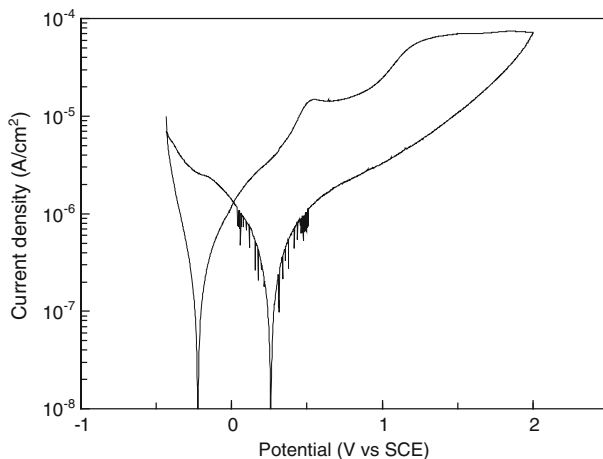
## Results and discussion

Figure 1 shows the variation of OCP as a function of immersion time for the TNZT alloy in PBS solution. The OCP shows an increase towards noble values in the first 24 h of immersion, suggesting the formation of a stable oxide film in solution, following which the potential reaches a steady state up to the duration of the experiment studied.

Figure 2 shows the cyclic potentiodynamic profile of TNZT alloy in PBS solution. The alloy shows a slow



**Fig. 1** OCP variation as a function of time for TNZT alloy at 37 °C



**Fig. 2** Cyclic potentiodynamic profile of TNZT alloy at 37 °C

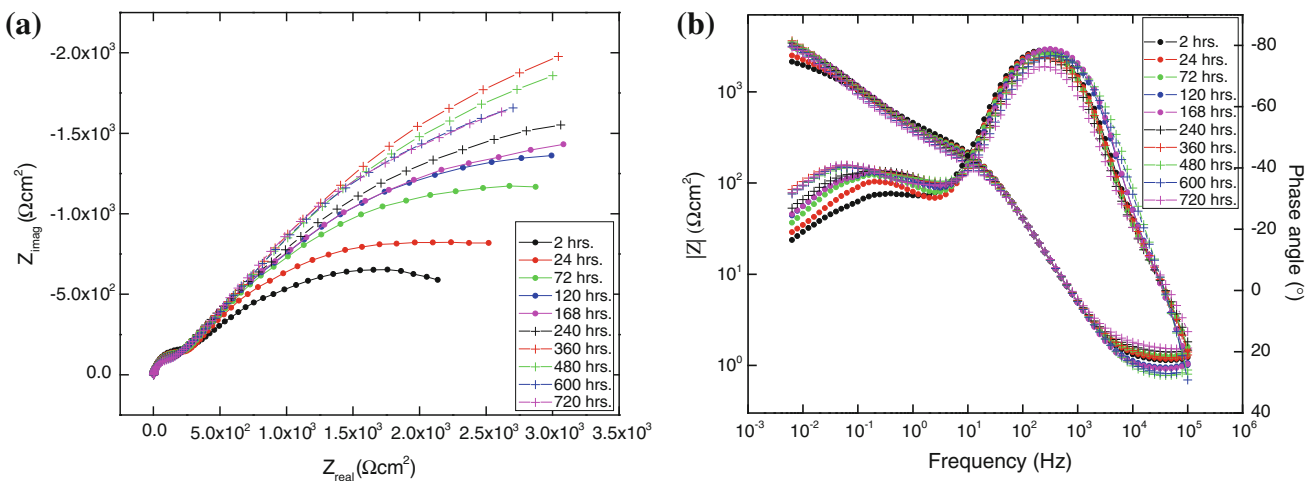
current increase in the active anodic region followed by a steadied current density in the passivation range which is observed even at 2 V, the maximum potential studied. At the vertex potential of 2 V, the curve starts to trace backwards and illustrates a rapid decrease and then a slow approach to zero. This is characteristic of valve metals and their alloys already passivated by their oxides [16].

Figure 3 shows the EIS plots for TNZT alloy at various immersion hours in PBS solution. The EIS data was fitted using the equivalent circuit shown in Fig. 4a which represents a duplex structure of the oxide formed over TNZT alloy.  $R_s$  is the solution resistance,  $R_p$  is the outer porous layer resistance, and  $CPE_p$  is the constant phase element of the porous layer.  $R_b$  is the inner barrier layer resistance and  $CPE_b$  is the constant phase element for the barrier layer. The impedance of CPE is given by Eq. 1

$$Z_{CPE} = Y_0^{-1}(j\omega)^{-n} \quad (1)$$

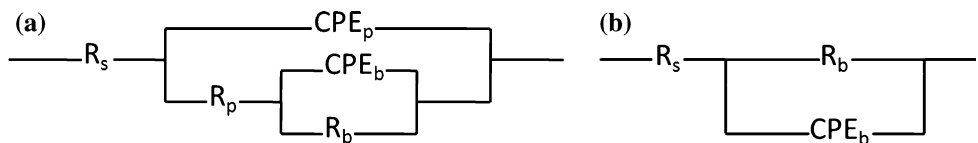
where  $\omega$  is the angular frequency in radians/s,  $Y_0$  is the admittance magnitude of the CPE, and  $n$  is the exponential term which can vary between 1 for pure capacitance and 0 for a pure resistor [17].  $n$  is a measure of surface inhomogeneity, the lower is its value, the higher is the surface roughening of the metal/alloy [18]. At all the immersion hours, two semicircles (Fig. 3a), two humps, and two inflexions (Fig. 3b) corresponding to the two time constant circuit model representative of the two-layer oxide can be clearly observed. Table 1 shows the EIS parameters for TNZT alloy at various immersion hours in PBS solution. Values for various parameters have been shown for selected intervals only. The values of the inhomogeneity parameter,  $n$  for the porous layer lie between 0.9 and 1 and thus a CPE has been used in place of a pure capacitor to account for surface inhomogeneity. In case of the barrier layer,  $n$  values are quite low, around 0.5, which might be due to the diffusive transfer of ions occurring at the barrier layer [19]. It has also been shown elsewhere that  $n$  values close to 0.5 need not necessarily be due to diffusion [19–21]. Deviation of  $n$  from the value of 1 for a pure capacitor is comprehended in terms of a non-normalizable distribution of relaxation times and it could also arise from non-uniform diffusion whose electrical analog is an inhomogeneously distributed RC transmission line [22].

Figure 5 shows the variation in barrier and porous layer resistance and capacitance values with increasing immersion hours at the OCP. The barrier layer resistance is an order of magnitude higher than the porous layer resistance and the barrier layer capacitance is two orders of magnitude higher than the porous layer capacitance (also seen in Table 1). This reveals that the outer porous layer is thicker (due to lower capacitance) and porous (due to lower resistance) and the inner barrier layer is thinner and less porous. It has been reported [23] that implant materials possessing a duplex



**Fig. 3** EIS Nyquist and Bode plots for TNZT alloy at various immersion hours at OCP and at 37 °C

**Fig. 4** Electrical equivalent circuit models used for EIS circuit modeling



**Table 1** EIS parameters for TNZT alloy at various immersion hours at OCP and at 37 °C

Time of immersion (h)	$R_s$ ( $\Omega \text{ cm}^2$ )	$\text{CPE}_p (\times 10^{-5}) [S(\text{srad}^{-1})^n/\text{cm}^2]$	$n_p$	$R_p$ ( $\Omega \text{ cm}^2$ )	$\text{CPE}_b (\times 10^{-3}) [S(\text{srad}^{-1})^n/\text{cm}^2]$	$n_b$	$R_b$ ( $\Omega \text{ cm}^2$ )
2	1.17	5.06	0.95	249.7	1.20	0.54	2744
24	1.23	5.00	0.95	247.8	1.24	0.61	3138
120	0.97	4.50	0.96	194.3	1.13	0.56	6067
240	1.46	5.11	0.94	187.4	1.13	0.57	6050
480	0.78	5.10	0.94	165.7	1.21	0.54	9400
720	1.59	6.15	0.92	160.7	1.42	0.54	8547

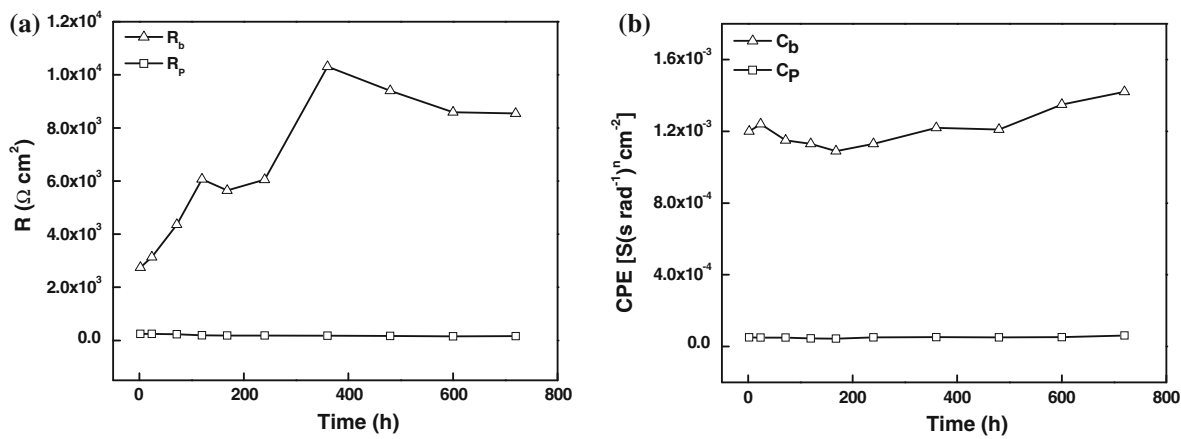
layer passive film with an inner barrier and outer porous layer display better osteointegration due to the migration of bone cells present in the body environment into the pores of the passive film, facilitating adhesion between the implant and the bone. The present results demonstrate the formation of a bilayer passive oxide film over TNZT alloy.

Figure 6 shows the EIS plots for TNZT alloy at various anodic potentials after 720 h of immersion in PBS solution. Table 2 shows the corresponding EIS parameters. At and above 300 mV, the two time constant circuit model was found to change to a one-time constant circuit model as shown in Fig. 4b.

Figure 6a–c compares the impedance plots at the OCP and various selected anodic step-up potentials such as 15, 60, 105, and 150 mV vs. OCP (−226, −181, −136, and −91 mV vs. SCE). Figure 6d–f compares the impedance plots at the OCP and selected higher anodic potentials. Figure 7 is a graphical representation of Table 2 and shows

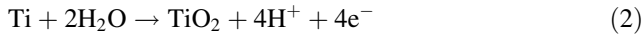
the variation in the barrier and porous layer resistance and capacitance values with increasing anodic potentials starting from the OCP up to 2 V at 720 h of immersion.

As can be observed, both from Fig. 6a–c as well as Table 2, the porous layer resistance increases and the barrier layer resistance decreases with increase in anodic voltage. This can be attributed to the transformation of a part of the barrier layer into the outer porous layer. The overall resistance of the two layers decreases with increase in anodic potential. This is due to an increase in current density in the active anodic region as seen in the polarization curve in Fig. 2. This increase may be due to the dissolution of any one of the alloying elements as has been already reported in case of TNZT alloy [10]. The increase in current density could also be due to the relatively high scan rate used due to which the thickening of the oxide film (composed of oxides of Ti, Nb, Zr, and Ta) would be insufficient to compensate for the high field effects of the



**Fig. 5** Resistance and capacitance of the oxide formed over TNZT alloy as a function of immersion time at OCP and at 37 °C

overpotential [24]. It has been shown that in case of titanium which is present as the dominant element in the alloy, in the active region, the growth of a uniform oxide film begins mainly as  $\text{TiO}_2$  [25, 26]:



$\text{Ti}_2\text{O}_3$  may also be formed but being an unstable species is again oxidized to  $\text{TiO}_2$  [27]:



At around 500 mV potential, the polarization curve shows a slight decrease in current density due to a decrease of the real surface area as the film thickness increases and the alloy starts to show a passive behavior. An increase in current density follows and continues to another passive region up to 2 V.

Due to the high field effects of the overpotential in the active anodic region, a noticeable large decrease in  $R_b$  is observed at the first step-up potential in the anodic range compared to OCP. The decrease in  $R_b$  continues thereafter up to 300 mV. Correspondingly the  $R_p$  values show an increase but the increase is not as significant as that in case of  $R_b$ . The decrease in  $R_b$  is as a result of dissolution of one or more of the alloying elements present in TNZT which makes the barrier layer porous and defective and subsequently a part of the outer porous layer. Due to the porosity, the increase in the resistance of porous layer is not tremendous. However, a decrease is observed in the capacitance values of both the barrier and the porous layers. This implies that the thickness of both the layers increases regardless of a decrease in  $R_b$  and an increase in  $R_p$ . This is understandable for  $R_p$ , in which case the barrier layer transforms into the porous layer, thus making the outer layer thicker. But an increase in barrier layer thickness implies that in addition to increased dissolution of the alloying elements, the formation of the oxides of these

elements also does occur (for example as shown in Eq. 2 for titanium). The oxide formation and dissolution together gives rise to a thicker but defective barrier layer. Another point to be noticed is that the thickening of the outer porous layer (also shown later in Fig. 8a) corresponding to a decrease in its capacitance in Fig. 7d and an increase in its resistance in Fig. 7b is more pronounced at the first step-up potential as compared to subsequent higher anodic potentials. This effect has already been observed by other authors [11, 28]. This behavior directly correlates to an abrupt decrease in  $R_b$  at the first step-up potential and the above mentioned hypothesis that the barrier layer is getting transformed into the outer porous layer. These changes observed at the first step-up potential are abrupt compared with the higher anodic potentials due to the sudden high field effects of overpotential at the high scan rate used from an initial stable oxide growth at the open circuit potential.

In Fig. 6d–f, it can be observed clearly at 300 mV that the semicircle size and impedance modulus show a decrease in the impedance curves compared to those at the OCP. Moreover, the impedance response changes from a two time constant to a one-time constant one at 300 mV and higher potentials. At further higher potentials, the size of the semicircle and the impedance modulus continues to increase, thereby suggesting the passive oxide formation over the alloy surface corresponding to the passive anodic region in the polarization curve. This can also be noticed in the increase in  $R_b$  values with increasing higher potentials in the bottom part of Table 2. A corresponding decrease in the capacitance of the barrier layer is also observed at 300 mV which appears as another abrupt decrease from  $-91$  mV in Fig. 7c. The decrease in capacitance follows at subsequent higher potentials up to 2 V. The decrease in capacitance in addition to an increase in resistance observed at the potential values approaching passivity implies the formation of both a thick as well as a protective

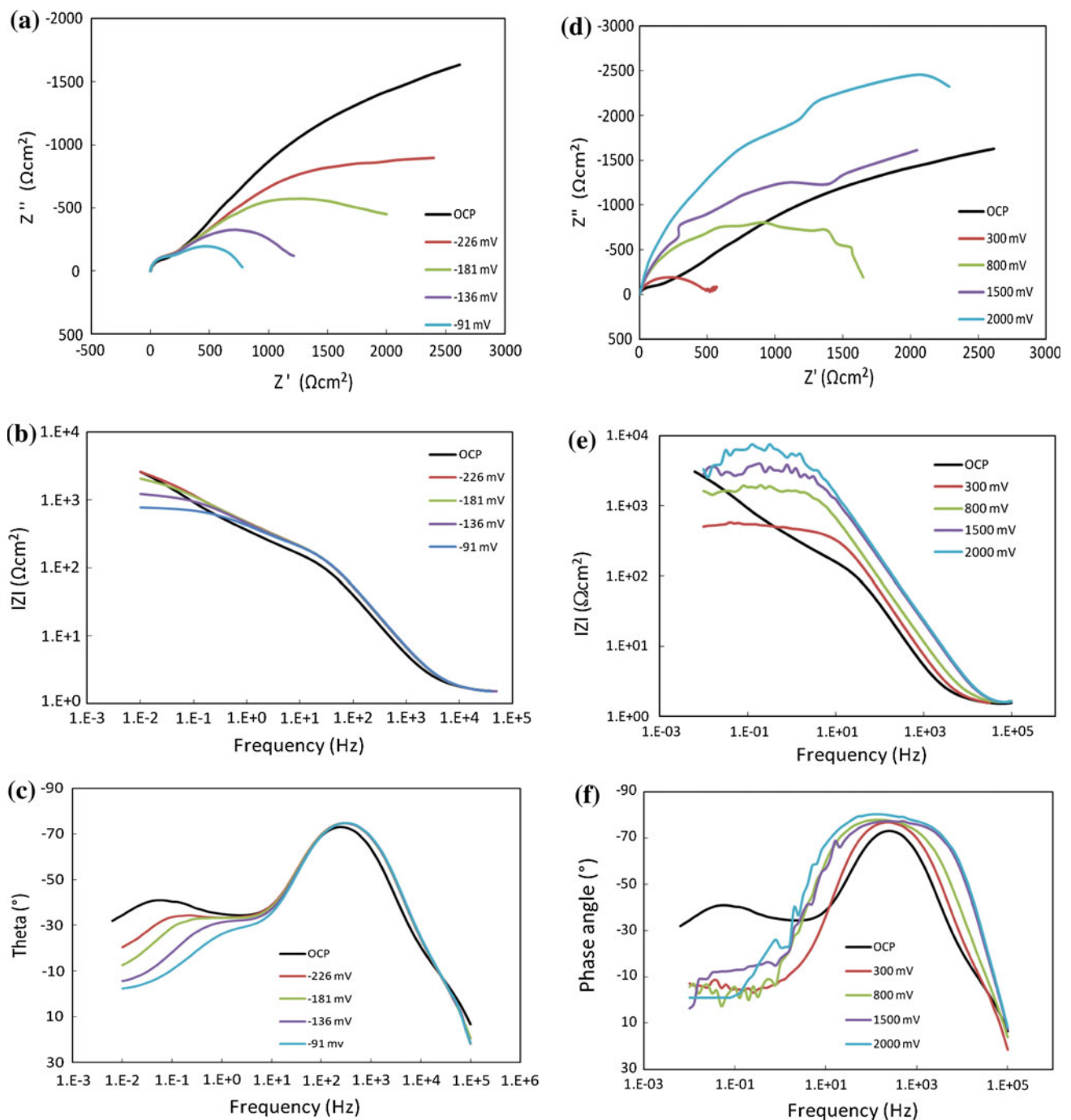


**Fig. 6** EIS plots at various anodic potentials in the active and passive regions for TNZT alloy at 37 °C

barrier layer as compared to the formation of a thick but defective barrier layer formed in the anodic potentials lying in the active region.

From the values of the capacities obtained at each potential, the thickness of each layer was calculated using Eq. 4 [29].

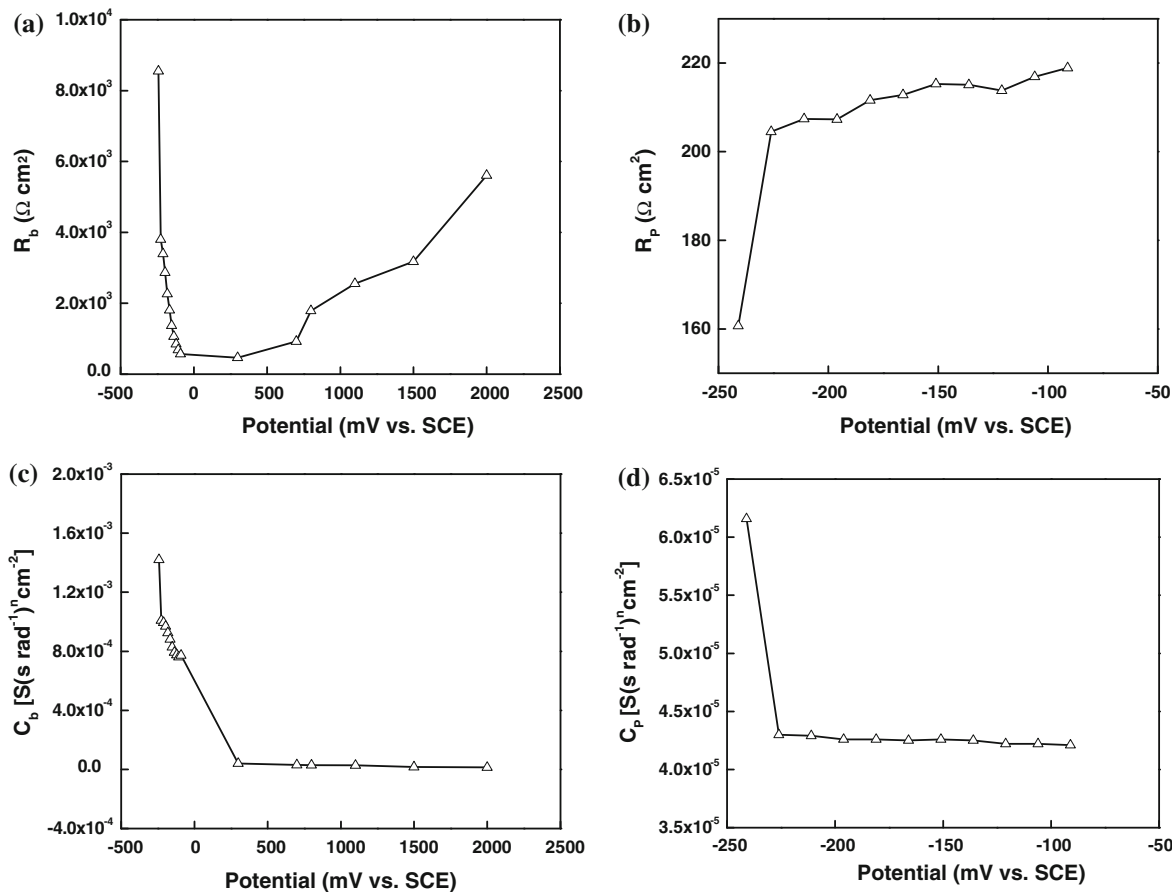
$$d = \varepsilon \varepsilon_0 A / C \quad (4)$$

where  $d$  is the thickness of the oxide layer,  $A$  is the surface area,  $C$  is the oxide layer capacitance,  $\varepsilon$  is the dielectric constant of the oxide, and  $\varepsilon_0$  is the permittivity of free space ( $=8.85 \times 10^{-12} \text{ F m}^{-1}$ ).

Equation 5 [29] has been used directly to calculate the overall oxide thickness (summation of the thicknesses of both layers).

**Table 2** EIS parameters for TNZT alloy at various anodic potentials at 37 °C

Potential (mV vs. SCE)	$R_s$ ( $\Omega \text{ cm}^2$ )	$CPE_p (\times 10^{-5}) [S(\text{srad}^{-1})^n/\text{cm}^2]$	$n_p$	$R_p (\Omega \text{ cm}^2)$	$CPE_b (\times 10^{-3}) [S(\text{srad}^{-1})^n/\text{cm}^2]$	$n_b$	$R_b (\Omega \text{ cm}^2)$
-241 (OCP)	1.59	6.15	0.92	160.7	1.42	0.54	8547
-226 (15 mV vs. OCP)	1.58	4.30	0.93	204.5	1.01	0.55	3802
-181 (60 mV vs. OCP)	1.59	4.26	0.93	211.6	0.92	0.59	2261
-136 (105 mV vs. OCP)	1.58	4.25	0.93	215.3	0.83	0.64	1367
-91 (150 mV vs. OCP)	1.58	4.21	0.93	218.9	0.77	0.70	569.7
300	1.58	—	—	—	0.040	0.92	462.1
800	1.62	—	—	—	0.029	0.91	1790
1500	1.55	—	—	—	0.016	0.90	3174
2000	1.57	—	—	—	0.013	0.92	5608

**Fig. 7** Resistance and capacitance of the oxide formed over TNZT alloy as a function of potential at 37 °C

$$d = \epsilon\epsilon_0 A 2\pi f (Z - Z_0) \quad (5)$$

where  $f$  is the frequency where the phase angle approaches  $-90^\circ$ ,  $Z$  is the impedance at frequency  $f$ , and  $Z_0$  is the impedance at high frequencies (solution resistance). Birch and Burliegh [30] have used Eq. 5 to calculate the oxide thickness from impedance data by approximating the oxide film to a capacitor.

Published literature [31–34] reports various values of the dielectric constants between 48 and 110. For the present work, a dielectric constant value of 50 was used to carry out the calculations for the oxide film thickness.

The film thickness for both the inner and outer oxide layers calculated using Eq. 4 at various anodic potentials has been plotted in Fig. 8. The first point in Fig. 8a and b corresponds to the OCP. In Fig. 8a, the outer porous layer

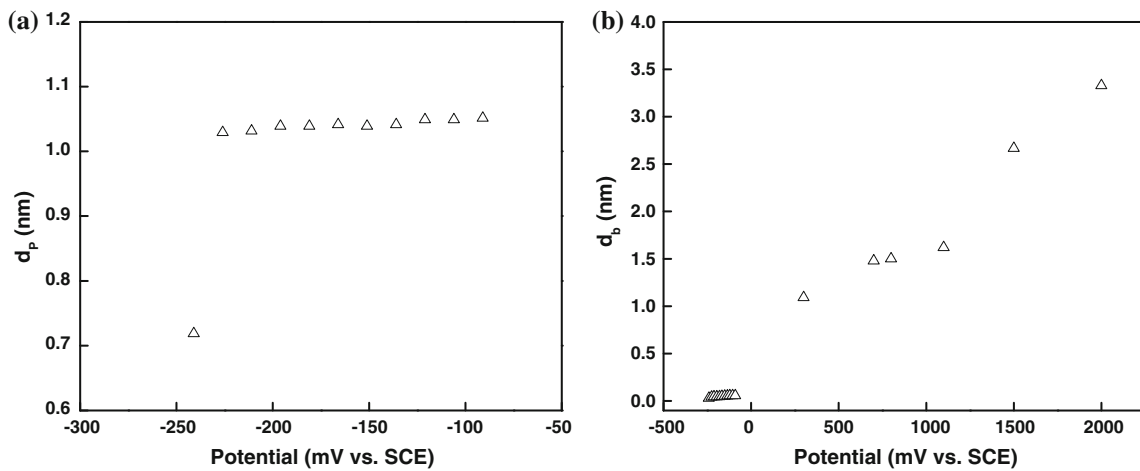


**Fig. 8** Thickness of the **a** outer porous and **b** inner barrier layer oxide film formed on TNZT alloy at 37 °C calculated using Eq. 4

shows a rapid increase in the thickness value from the OCP to the first step-up potential value in the anodic region and subsequently, the thickness shows a linear behavior with a very small slope value. This complements the corresponding increase in  $R_p$  and a decrease in  $C_p$  observed in Fig. 7b and d from OCP to the first step-up potential. The slope, on the other hand, for  $d_b$  versus potential curve is comparatively much larger.

The sum of the inner barrier and the outer porous layer thickness values calculated using Eq. 4 and shown separately in Fig. 8a and b has been plotted as a function of potential in Fig. 9. It is worth to mention that at all the potentials below 300 mV, the total thickness is the sum of the individual thickness values of the two layers (calculated individually from their respective capacities using Eq. 4)

and at 300 mV and above, the total thickness is the thickness of only the inner barrier layer (calculated from the capacities of the barrier layer using Eq. 4). Equation 5 directly gives the overall thickness of the oxide film at various anodic potentials, which has also been shown in the same graph for comparison. There is a fairly good agreement between the oxide thickness calculated using the two methods. The thickness values of the inner barrier and the outer porous layers calculated using Eq. 4 were found to increase with increase in anodic potentials throughout at both low and high overpotentials, which supports the observed decrease in capacitance observed with increasing anodic potentials in Table 2 and in Fig. 7c and d. The oxide film thickness is several nanometers and follows more or less a linear trend with potential. The values obtained for TNZT are in accordance with the thickness values reported (1–10 nm) for titanium alloys in a simulated body fluid for a similar anodic potential range [29, 34].

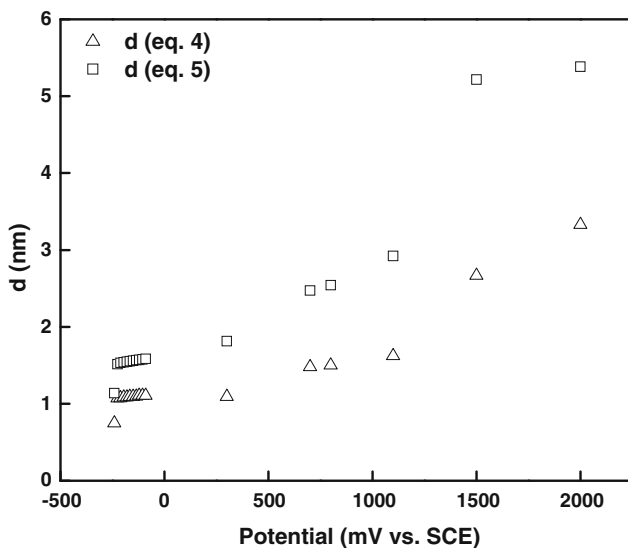


**Fig. 9** Thickness of the oxide film formed on TNZT alloy at 37 °C

## Conclusions

The Ti–35.5Nb–7.3Zr–5.7Ta  $\beta$  alloy displays a two time constant electrochemical impedance response at various immersion hours at the OCP, which indicates the presence of an inner barrier and an outer porous oxide layer over its surface. The bilayer structure of the oxide can be used to promote osteointegration in implant applications. However, at higher anodic potentials in the passive range, the alloy displays a one-time constant impedance response for a single compact oxide layer, an increase in the resistance of the oxide and a simultaneous decrease in its capacitance. The thickness of the oxide formed increases with increase in anodic potential.

## References

1. Banerjee R, Nag S, Stechschulte J, Fraser HL (2004) Biomaterials 25:3413
2. Nag S, Banerjee R, Stechschulte J, Fraser HL (2005) J Mater Sci Mater Med 16:679
3. Nag S, Banerjee R, Fraser HL (2005) Mater Sci Eng C 25:357
4. Wagner K (1991) Clin Orthop 271:12
5. Okazaki Y, Rao S, Ito Y, Tateishi T (1998) Biomaterials 19:1197
6. Jatsy M (1993) J Appl Biomater 4:273
7. Milosev I, Antolic V, Minovic A, Cor A, Herman S, Pavlovic V, Campbell P (2000) J Bone Joint Surg Br 82-B:352
8. Brunette DM, Tengvall P, Textor M, Thomsen P (2001) Titanium in medicine: material science, surface science engineering biological responses and medical applications. Springer, Germany, p 25
9. Zardiackas LD, Kraay MJ, Freese HL (2005) Titanium, niobium zirconium and tantalum for medical and surgical applications. ASTM International, PA, USA, p 3
10. Karthega M, Raman V, Rajendran N (2007) Acta Biomater 3:1019
11. Valereto ICL, Wolyne S, Ramires I, Guastaldi AC, Costa I (2004) J Mater Sci Mater Med 15:55
12. Ahmed TA, Long M, Silverstri J, Ruiz C, Rack HJ (1996) A new low modulus, biocompatible titanium alloy. In: Blenkinsop PA, Evans WJ, Flower HM (eds) Titanium'95. The Institute of Materials, p 1760
13. Niinomi M, Kuroda D, Fukunaga K, Morinaga M, Kato Y, Yashiro T, Suzuki A (1999) Mater Sci Eng A263:193
14. Okazaki Y, Ito Y, Kyo K, Tateishi T (1996) Mater Sci Eng A213:138
15. Raman V, Nagarajan S, Rajendran N (2006) Electrochim Commun 8:1309
16. Marino CEB, de Oliveira EM, Rocha-Filho RC, Biaggio SR (2001) Corros Sci 43:1465
17. Hsu CH, Mansfeld F (2001) Technical note: concerning the conversion of the constant phase element parameter ( $Y_0$ ) into a capacitance. Corrosion 57:747
18. Chongdar S, Gunasekaran G, Kumar P (2005) Electrochim Acta 50:4655
19. Popova A, Raicheva S, Sokolova E, Christov M (1996) Langmuir 12:2083
20. Rammelt U, Reinhart G (1987) Corros Sci 27:373
21. Armstrong RD, Dickinson TD, Willis PM (1974) J Electroanal Chem Interfacial Electrochem 53:389
22. Shukla AK, Balasubramaniam R (2006) Corros Sci 48:1696
23. Badawy WA, Fathi AM, El-Sherief RM, Fadl-Allah SA (2009) J Alloys Comp 475:911
24. de Luiz Sergio A, Isolda C (2007) Mater Res 10:293
25. Blackwood DJ, Peter LM (1989) Electrochim Acta 34:1505
26. Abdel-Rahim MA (1995) J Appl Electrochem 25:881
27. Pourbaix M (1974) Atlas of electrochemical equilibria in aqueous solutions. NACE, Houston
28. Milosev I, Kosec T, Strehblow H-H (2008) Electrochim Acta 53:3547
29. Ibris N, Mirza Rosca JC (2002) J Electroanal Chem 526:53
30. Birch JR, Burleigh TD (2000) Corrosion 56:1233
31. Marsh J, Gorse D (1998) Electrochim Acta 43(7):659
32. Serruys Y, Sakout T, Gorse D (1993) Surf Sci 282:279
33. Blackwood DJ (2000) Electrochim Acta 46:563
34. Ohtsuka T, Otsuki T (1998) Corros Sci 40:951